Modeling the Response of 3D Textile Composites under Compressive Loads to Predict Compressive Strength

M. Pankow[1], A.M. Waas[2] and C.F. Yen[3]

Abstract: The compression response of 3D woven textile composites (3DWC) that consist of glass fiber tows and a polymer matrix material is studied using a combination of experiments and finite element based analyses. A previous study reported by the authors consisted of an experimental investigation of 3DWC under high strain rate loading, Pankow, Salvi, Waas, Yen, and Ghiorse (2011). Those experimental results were explained by using the finite element method to analyze the high rate deformation response of representative volume elements (RVEs) of the 3DWC, Pankow, Waas, Yen, and Ghiorse (2012). In this paper, the same modeling strategy is used to examine the quasi-static, compressive deformation response of 3DWC. The effect of using different numbers of the textile repeat unit architecture in the RVE, on the predicted compression strength, is examined. The transitions in failure modes that are seen in experiments are seen to be captured by the model that is presented here.

Keywords: 3D Woven, RUC Modeling, Material Characterization,

1   Introduction

3D woven textile composites (3DWCs) are gaining ubiquity in manufactured goods. The tailorability of the architecture allows for the development and design of a variety of materials for a diverse array of applications. Many of these architectures, and the challenges associated with the manufacturing process have been previously discussed in Bogdanovich and Mohamed (2009).

Classical methods, such as classical laminated plate theory (CLPT) Jones (1999), derived for laminated composites have shown promising results for 2D tape laminates. However these theories do not facilitate a straight-forward extension to

---

[1] Composite Structures Laboratory, Department of Aerospace Engineering, University of Michigan, 1320 Beal Street, Ann Arbor, MI 48109-2140, USA
[2] Corresponding author. Email: dcw@umich.edu
[3] Army Research Laboratory, Aberdeen, MD, USA

3DWCs because of the deviations from planar interfaces that are characteristic of 3DWCs. Extensions of CLPT to model 2D woven Raju and Wang (1994) and 3D woven Pankow, Waas, Yend, and Ghiorse (2009) laminates have been implemented. These models are typically good at predicting linear elastic macroscopic response, but they lack the fidelity to accurately capture local stress and strain fields. The inter-plane movement of fibers often a Z-fiber, is typically the hardest constituent to model accurately and many have attempted to derive special elements or ways of handling this movement Talbi, Batti, Ayad, and Guo (2009). When the textile architecture is "homogenized", mechanism based failure modeling which is necessary for capturing the effects of constituents and local geometry on the observed failure mechanism, becomes out-of-reach, Quek and Waas (2003); Quek, Waas, Shahwan, and Agaram (2003); Song (2007). Specialized codes Kamiya, Cheeseman, Popper, and Chou (2000) that are aimed at capturing specific mechanisms have been developed, but these approaches may not provide the level of fidelity that is needed to understand the influence of the textile architecture, constituent material properties and manufacturing imperfection signature.

3D finite element models with varying degrees of refinement have been developed in the past to more accurately capture stress concentrations, and non-linear material and geometric behavior Lomov, Ivanov, Verpoest, Zako, Kurashiki, Nakai, and Hirosawa (2007); Song, Waas, Shahwan, Xiao, and Faruque (2007). Initial models of the braided textile architectures produced good correlations, and included manufacturing induced effects such as tow consolidations Song (2007); Sejnoha and Zeman (2008); Robitaille, Long, Jones, and Rudd (2003). The representative unit cell approach has been the most widely adopted method of performing mechanical response characterization Yen and Caiazzo (2001); Tan, Tong, and Steven (2000, 1998); Tan and Steven (1997); Zeng, Wu, and Guo (2004); Shahkarami and Vaziri (2007); McGlockton, Cox, and McMeeking (2003); Schwer and Whirley (1999); Ji and Kim (2007); Quek, Waas, Shahwan, and Agaram (2004). However early models for 3DWC used simplifications such as neglecting the Z-fiber crowns, or fitting everything into a building block approach within a grid system Tan, Tong, Steven, and Ishikawa (2000); Tan, Tong, and Steven (1998), which eliminates the binding and stress concentration due to the Z-fiber. Other approaches have examined sub-cell methods to represent the complex architecture that occurs within a RVE Zeng, Wu, and Guo (2004), but this requires a complex calibration of each subcell.

---

[0] The term "fibers" is used to refer to fiber tows, that consists of many thousands of fibers held by the matrix material

[0] The manufacturing imperfection signature is unique to the type of method that is used to produce the 3DWC, hence it can, for example introduce unintended deviations to the textile architecture which can influence the subsequent in-service deformation response of the material Song, Waas, Shahwan, Xiao, and Faruque (2007)

In order to accurately capture stress concentrations and unintended manufacturing induced imperfections due to weaving, detailed 3D models of the actual woven architecture must be investigated. Accurate models of tri-axially braided 2D laminates have shown a strong correlation to experimental data Quek, Waas, Shahwan, and Agaram (2003); Song (2007). The results reported showed an accurate representation of the macroscopic stress-strain response at the RVE level Song, Waas, Shahwan, Faruque, and Xiao (2008) and an ability to predict the mechanism of failure and associated strength, the latter being a challenging task.

In this paper, models of 3DWC have been examined within a finite element based modeling framework, motivated by earlier studies, Pankow, Waas, Yen, and Ghiorse (2012), and also on quasi-static experimental results reported here. Many aspects of the deformation response, including comparisons with experiments, transitions in the failure mechanism as a function of loading rate, and the effect of the number of repeat units within the representative volume that is studied computationally, are all examined.

2   Material

The material used in this study is a 6% Z-fiber reinforced 3D woven composite. A model of the architecture can be seen in figure 1, where details have been previously reported, Pankow, Waas, Yen, and Ghiorse (2012). The material uses S2 glass fibers and SC-15 epoxy, a thermoset polymer, for the matrix material. The mechanical properties of the glass fibers are reported in table 1 which are obtained from, Herakovich (1998).

Table 1: S-2 glass fiber properties Herakovich (1998)

E_{11} (GPa)	G_{12} (GPa)	v_{12}
114.2	46.5	0.22

3   Proposed models.

Details for developing the RVE finite element model were obtained through the use of both optical measurements through a microscope and from μCT imaging, see figure 2. Dimensions were measured from each of the techniques to find average dimensions of the tow geometry. The average dimensions are given in table 2. A solid model of the textile architecture was created and imported into ABAQUS. The model consists of 70,000 tetrahedral elements. The choice of model size was
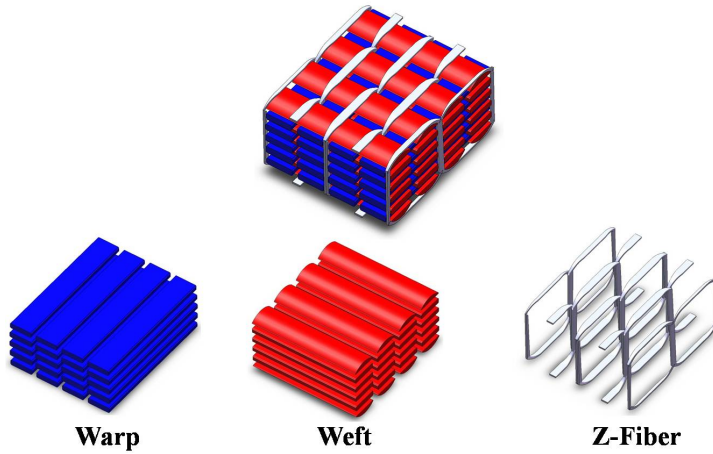
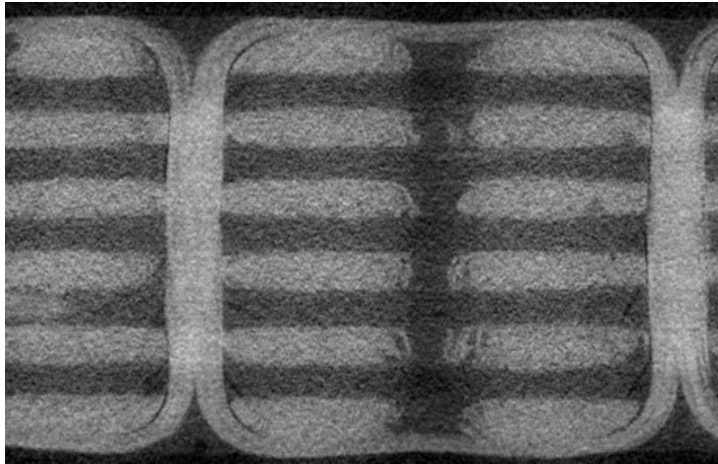Figure 1: Representative Geometry of 3D woven RUC geometry.

based on earlier results that showed convergence, in connection with simulations of the dynamic computational results, Pankow, Waas, Yen, and Ghiorse (2012).

Table 2: Sample Geometry of RUC and constituents

	Width (mm)	(in.)	Length (mm)	(in.)	Thickness (mm)	(in.)	Distance between Fibers (mm)	(in.)
RUC	6.80	.2676	8.03	0.3162	7.29	.2872		
Warp	2.71	0.1065	8.03	0.3162	0.63	0.0248	0.69	0.0273
Weft	3.11	0.1225	6.80	0.2676	0.60	0.0235	0.90	0.0356

Because the tows are impregnated with a polymer that shows nonlinearity in its stress-strain response, the homogenized transverse properties of the fiber tows will also display nonlinear material behavior. This material nonlinearity is captured through an anisotropic, Hill type plastic potential, Song, Waas, Shahwan, Faruque, and Xiao (2009), which is,
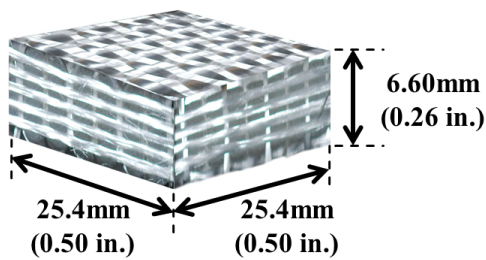
$$f(\sigma) =$$
$$\sqrt{F(\sigma_{22} - \sigma_{33})^2 + G(\sigma_{22} - \sigma_{11})^2 + H(\sigma_{11} - \sigma_{22})^2 + 2L\sigma_{23}^2 + 2M\sigma_{31}^2 + 2N\sigma_{12}^2}$$

$$(1)$$

(a) μCT image of architecture
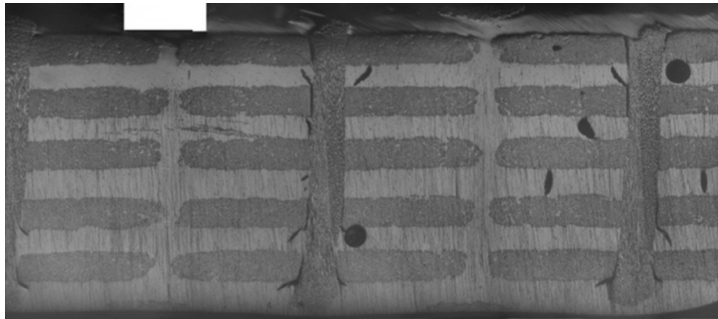
(b) Microscope image of architecture

6.60mm
(0.26 in.)

25.4mm   **25.4mm**
(0.50 in.)   **(0.50 in.)**

(c) Matrix burn off image of architecture

Figure 2: Representative Geometry of 3D woven RUC geometry.

where the 1 direction refers to the fiber direction and the 2 and 3 are transverse to the fiber. The constants $F, G,\ldots N$ are defined as

$$
\begin{aligned}
F &= \frac{(\sigma^0)^2}{2}\left(\frac{1}{\sigma_{22}^2}+\frac{1}{\sigma_{33}^2}-\frac{1}{\sigma_{11}^2}\right)=\frac{1}{2}\left(\frac{1}{R_{22}^2}+\frac{1}{R_{33}^2}-\frac{1}{R_{11}^2}\right)\\
G &= \frac{(\sigma^0)^2}{2}\left(\frac{1}{\sigma_{33}^2}+\frac{1}{\sigma_{11}^2}-\frac{1}{\sigma_{22}^2}\right)=\frac{1}{2}\left(\frac{1}{R_{33}^2}+\frac{1}{R_{11}^2}-\frac{1}{R_{22}^2}\right)\\
H &= \frac{(\sigma^0)^2}{2}\left(\frac{1}{\sigma_{11}^2}+\frac{1}{\sigma_{22}^2}-\frac{1}{\sigma_{33}^2}\right)=\frac{1}{2}\left(\frac{1}{R_{11}^2}+\frac{1}{R_{22}^2}-\frac{1}{R_{33}^2}\right)\\
L &= \frac{3}{2}\frac{\tau^0}{\sigma_{23}}^2=\frac{3}{2}\frac{1}{R_{23}}^2\\
M &= \frac{3}{2}\frac{\tau^0}{\sigma_{31}}^2=\frac{3}{2}\frac{1}{R_{31}}^2\\
N &= \frac{3}{2}\frac{\tau^0}{\sigma_{12}}^2=\frac{3}{2}\frac{1}{R_{12}}^2
\end{aligned}
\tag{2}
$$

where σ^0 is the reference yield stress, and τ^0 is the reference shear yield stress. It follows that,

$$
\begin{aligned}
R_{11} &= \frac{\sigma_{11}}{\sigma^0}\\
R_{22} &= \frac{\sigma_{22}}{\sigma^0}\\
R_{33} &= \frac{\sigma_{33}}{\sigma^0}\\
R_{12} &= \frac{\sigma_{12}}{\tau^0}\\
R_{13} &= \frac{\sigma_{13}}{\tau^0}\\
R_{23} &= \frac{\sigma_{23}}{\tau^0}
\end{aligned}
\tag{3}
$$

Since the individual yield stress ratios, R_{ij}, corresponding to the different individual stress states are not known a priori, it is assumed that the R_{ij}'s scale according to the corresponding moduli ratios. Thus, it is assumed that,

$$R_{11} = \frac{E_{11}}{E^0}$$

$$R_{22} = \frac{E_{22}}{E^0}$$

$$R_{33} = \frac{E_{33}}{E^0}$$

$$R_{12} = \frac{E_{12}}{G^0}$$

$$R_{13} = \frac{E_{13}}{G^0}$$

$$R_{23} = \frac{E_{23}}{G^0} \tag{4}$$

The elastic tow properties, $E_{11}, E_{22}, E_{33}, G_{12}, G_{13}$ and G_{23} are calculated using the CCM model Pankow, Waas, Yend, and Ghiorse (2009), and are shown in Table 3, where the glass fiber elastic modulus used is 114.2 GPa and poisson ratio is 0.22, while the corresponding matrix elastic properties are 2.48 GPa and 0.36. The non-linear uniaxial matrix stress-strain response curve (SC-15) is shown in Figure 3, and this is used as the effective stress-strain response for scaling the plastic properties. Thus, E^0 and G^0 in the above expressions are the matrix Youngs modulus and shear modulus respectively. For SC-15 these are, $E^0 = 2.48GPa$ and $G^0 = 0.912GPa$. It is to be noted that using the matrix uniaxial stress-strain response and the CCM model expression for E_{22}, a nonlinear uniaxial stress-strain response curve for the fiber tows (with a fiber volume fraction of 57.6%) can be constructed assuming that the matrix can be represented as a secant solid in the nonlinear regime. That is, beyond the proportional limit, the matrix is assumed to be a solid with a secant modulus, $E_m(\sigma_c)$, where σ_c is the fiber tow, composite transverse stress. This composite stress-strain response is shown in Figure 4, designated as "CCM Plasticity", and is compared against a similar response curve that is obtained by scaling the pure matrix stress values by the ratio, $\frac{E_{22}}{E^0}$. This latter curve, designated as "modulus ratio" agrees remarkably well with the "CCM Plasticity" curve, suggesting that using the uniaxial stress-strain response of the matrix in the anisotropic plasticity model for the tows as the reference stress-strain response is convenient and produces the same effects as using the "2" direction (transverse) effective stress-strain response as the reference.

4 Quasi-Static Experimental Results

Compression tests were carried out at a rate of 0.01 mm/sec (0.0004 in/sec) on a hydraulically activated load frame. Specimens measured $12.7mm(0.500in.)$ by

Table 3: 6% Z-fiber modeling parameters

	Warp		Weft	
	GPa	ksi	GPa	ksi
E_{11}	62.58	9077	66.6	9658
E_{22}	6.08	882	6.57	953
E_{33}	6.08	882	6.57	953
ν_{12}	0.2718		0.2673	
ν_{13}	0.1899		0.1725	
ν_{23}	0.1899		0.1725	
G_{12}	2.90	421	3.19	463
G_{13}	2.55	370	2.80	406
G_{23}	2.55	370	2.80	406
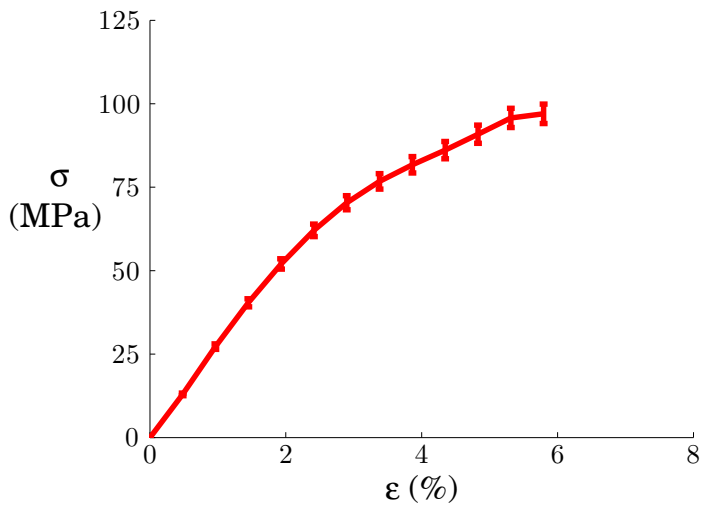
Figure 3: Quasi-static stress vs. strain curve for SC-15 matrix material.

12.7mm(0.500$in.$) and 6.60mm(0.260$in.$) thick. Five samples were tested in each orientation with a representative curve shown for each orientation; statistics are shown in table 4. The specimen dimensions corresponded to the specimens that
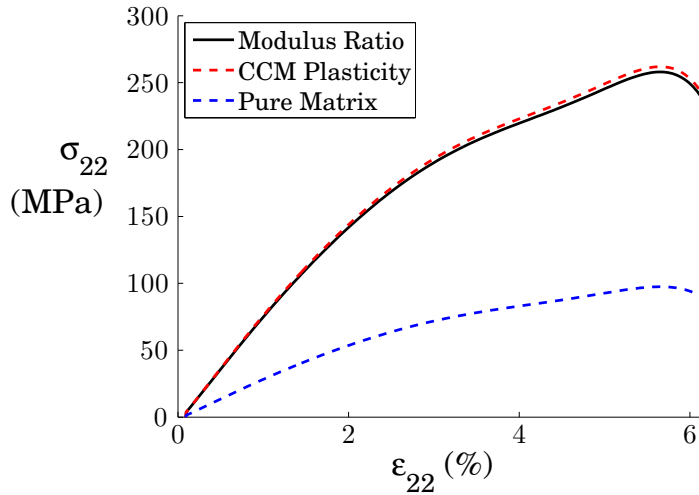
Figure 4: Comparison of the two different methods for calculating the stress vs. strain response of a fiber tow bundle in the transverse direction.

were also examined in the high rate compression studies reported in, Pankow, Salvi, Waas, Yen, and Ghiorse (2011). Figure 5 shows the compressive stress-strain response deduced from the test. Here, the macroscopic stress is the applied load divided by the specimens cross-sectional area while the macroscopic strain is the normalized (by the specimen length) end-shortening. The failure mechanism was kink band formation in the axial tows (which are aligned with the load axis). These can be seen in figure 6, where clear kink bands were formed in the samples. However, the warp specimens produced a slightly larger failure load, due to the fact that the kink band didn't form as readily as can be seen in figure 6. This is because the kink band, that forms at an angle, requires a minimum length of specimen for it to form in an unconstrained manner. This will become evident in the discussion later with larger specimen test results.

Figure 7 shows how the kink band forms at an angle of 45°. This angle formation is typical in all of the experimental results obtained at quasi-static rates, for both, weft and warp specimens. These bands are also seen in figure 6 which show two bands forming. However, as stated before, due to the small length, the bands that form are prevented from running across the entire specimen, therefore multiple bands are formed in the material. This suggests that if the kink band formation is constrained, the measured compression strength is elevated.
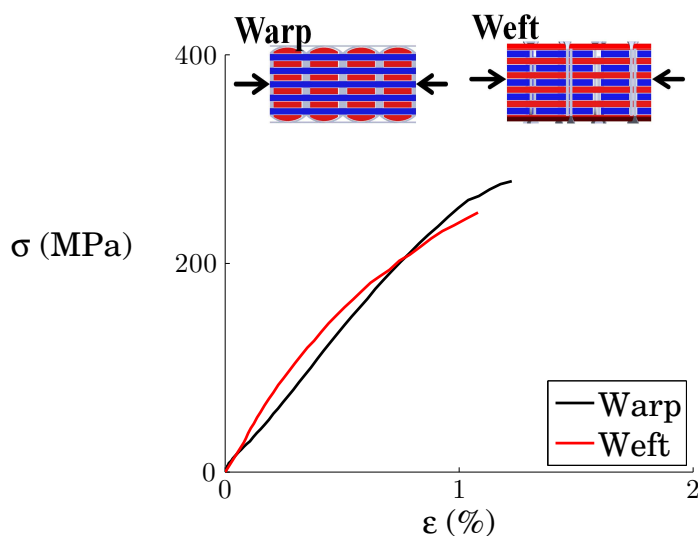
Figure 5: Quasi-static compression response of 6% Z-fiber reinforced composite Pankow, Salvi, Waas, Yen, and Ghiorse (2011).

Table 4: Strength Values

	Avg (MPa)	Std (MPa)
Warp	258	21
Weft	248	24

To investigate this further, larger specimens were examined to determine if the failure mode is influenced by specimen size. Test panels of 152.4 mm (6 in.) by 101.6 mm (4 in.) with a thickness of 6.6 mm (0.26 in.) were made. Specimens were placed in a compression fixture with anti-buckling guides to prevent premature failure, see figure 8. Two configurations were tested. An un-notched panel was tested along with a panel with notches cut in the center to promote failure in the center of the specimen (see figure 9. Three samples of each configuration have been tested with a representative response plotted for comparison. The macroscopic stress-strain response of the samples are shown in figure 10, which also shows a comparison against the smaller, SHPB type specimens. The statistical comparison of the samples can be seen in table 5. The weft direction results shows similar failure strengths with some variation in strains closer to failure. Similar stiffness

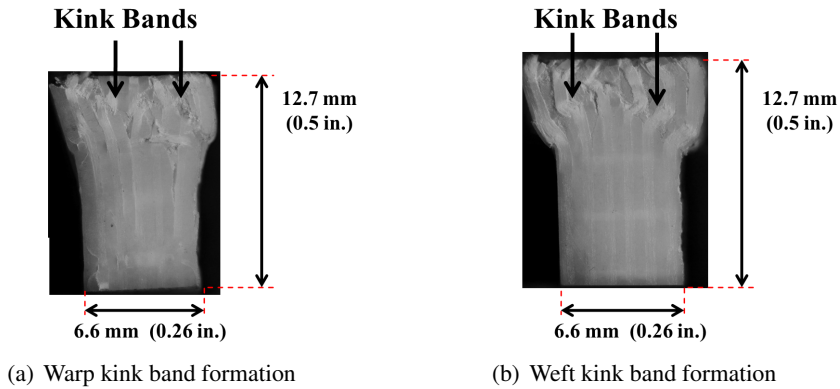(a) Warp kink band formation   (b) Weft kink band formation

Figure 6: Comparison of the quasi-static failure modes in the composite material. Pankow, Salvi, Waas, Yen, and Ghiorse (2011)
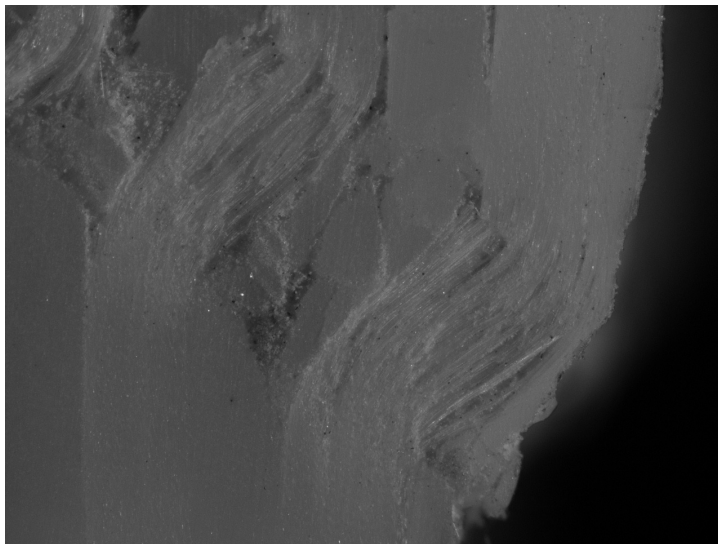

Figure 7: Microscopic images of kink bands obtained in the quasi-static compression tests Pankow, Salvi, Waas, Yen, and Ghiorse (2011).

are seen also. The warp direction results reproduce the same stiffness between the different sets of specimens, however the strength of the small specimen is seen to be elevated. The kink band which formed in the larger specimen is shown in figure 11. It should be noted that a single kink band is dominant at failure suggesting that the specimen size, if not large enough, can produce a change in the failure mode

(multiple bands seen in the smaller specimens) leading to an elevation in strength as discussed earlier. It should be noted here that the stress concentration produced from the notch did not influence the strength of the material much as the kink band never initiated from the notch, rather always in the middle of the specimen, occurring suddenly. Further investigation of this is needed, however due to limited amount of material available, this was not possible.
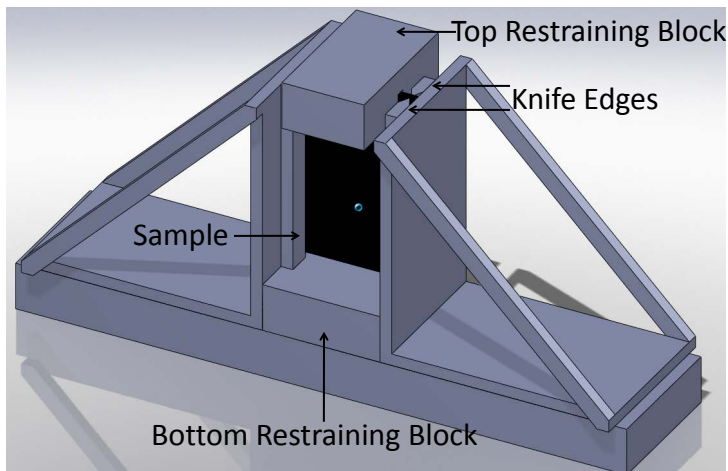

Figure 8: Large Compression fixture with anti-buckling guides.

Table 5: Strength Values

	Avg (MPa)	Std (MPa)
Warp	229	25
Warp Notch	217	19
Weft	259	11
Warp Notch	247	21
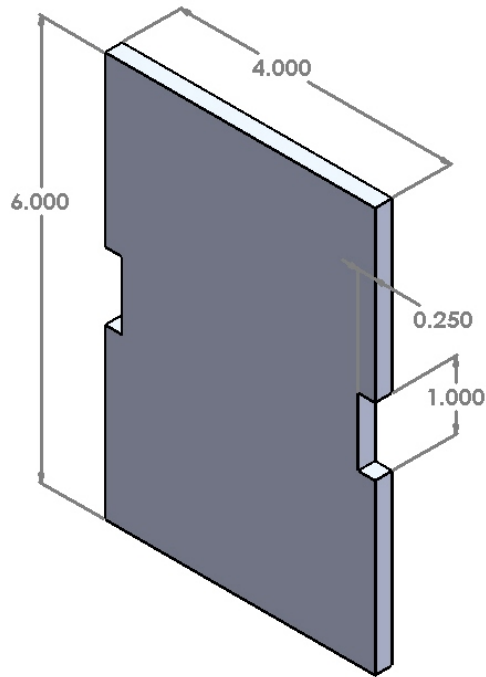
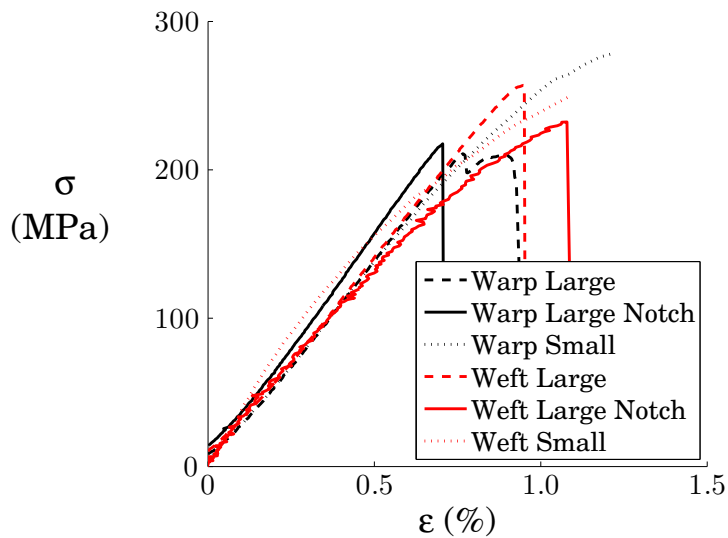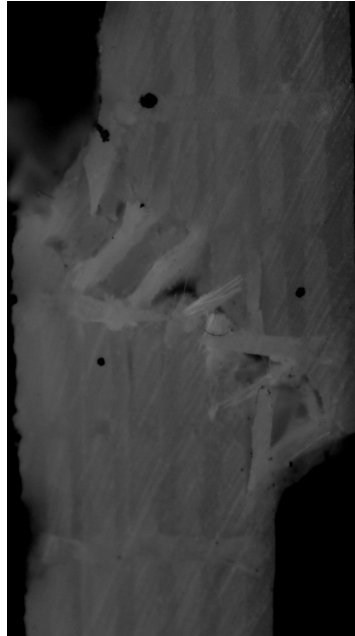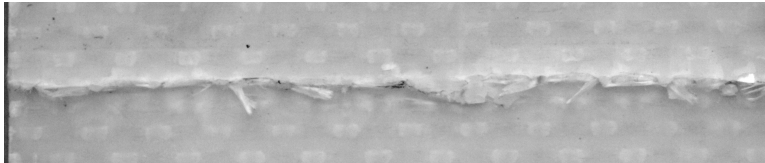Figure 9: Large compression sample with notch shown to promote failure in the gauge section.

Figure 10: Static compression test results for 6% Z-fiber reinforced composite material Pankow, Salvi, Waas, Yen, and Ghiorse (2011).

(a) Kink band formation in a large sample.

(b) Perpendicular surface to the kink band formation showing a single kink band that forms all the way across the specimen.

Figure 11: Weft specimen failed in kink band formation Pankow, Salvi, Waas, Yen, and Ghiorse (2011).

5   Computational Results

The computational model developed and used previously in Pankow, Waas, Yen, and Ghiorse (2012), was used to analyze the experimental results. The model was shown to produce the correct linear elastic stiffnesses for the warp and weft directions as discussed in Pankow, Waas, Yen, and Ghiorse (2012). The model represents the tows as elastic-plastic anisotropic solids as discussed earlier and the matrix as an elastic-plastic isotropic solid that conforms to the J2 incremental theory of plasticity with an associated flow rule. Details of developing the computational
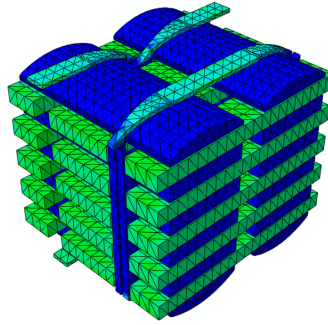
Figure 12: RVE of 3D woven geometry. The matrix material has been removed showing only the fiber tow bundles.

model are described in Pankow, Waas, Yen, and Ghiorse (2012). The RVE of the 3DWC that is computationally analyzed is shown in Figure 12. Initially, the local buckling modes of the RVE model were obtained and the buckling mode shape that corresponded to the lowest local buckling load was used to perturb the perfect RVE mesh. The amplitude of the imperfection shape was found to be x=2.5% for the warp and x=3.3% for the weft, conforming to the textile architecture, as described in Pankow, Waas, Yen, and Ghiorse (2012). The imperfect RVE model was then subjected to displacement control compression loading, incorporating nonlinear geometry, nonlinear material properties and in conjunction with the arc-length, RIKS solver available in the commercial software ABAQUS. The boundary conditions imposed on the specimen were that one side was fixed, while opposing face was subjected to displacement control, identical to how the experiments were run. All other surfaces were left free.

The macroscopic stress vs. macroscopic strain plots so obtained are shown in figure 13. It should be noted here that the yield stress of the individual tows in the axial direction is significantly larger than the other directions, with the assumed modeling that scales the R_{ij}'s according to the elastic stiffness values. In reality, slight undulations of the fibers within the tows would render this ratio to be smaller. However, it is still much larger than the other values as shown in table 6. Thus, R_{11} was set to 7, which is the ratio of the compression strength of a fiber tow to the yield stress in the matrix (corresponding to 48.5MPa). The compression yield strength of the tow was computed to be 340 MPa (49.2 ksi) and the ultimate strength was computed to be 800 MPa (116 ksi), based on analyzing a single fiber tow as described in Song, Waas, Shahwan, Faruque, and Xiao (2009). The effect of the matrix material properties on the initial elastic RVE properties is seen in figure 13, which shows

predictions for both measured material properties and also for a matrix material that yields at half of the measured yield strength ("Low Matrix"). It is seen that lowering the matrix yield stress makes very little difference in the predicted outcome for the macroscopic RVE stress-strain response, and in particular the load at which the RVE fiber tows form a kink band. The only noticeable result is for the post kinking loads.

Table 6: R_{ij} Values, where the ratio is based on the plastic properties of the pure matrix material

R_{11}	R_{22}	R_{33}	$R_{1}2$	R_{13}	R_{23}
7	2.5	2.5	3.04	2.68	2.68

The computational results show good agreement with the experimental data with respect to both the elastic moduli and the onset of failure in the material for the warp orientation. It predicts the onset of kink band formation, however the model does not capture the kink band angle that occurs in the experiment, but rather at a layer where it would occur at the location of the Z-fiber. The model also cannot capture the load drop associated with the onset of the kink band formation which is an instability in the material. This suggests that the 1 RUC approach may not be accurate for predicting the overall response in the warp direction. It should also be noted that previously the onset of failure was predicted at delaminations with fiber brooming in the samples at the higher rates, see figure 13. However, at the quasi-static rates analyzed here, kink band formation was predicted in the material and is also seen in the experiments. This transition in failure mode was accurately captured in the computational model. This transition is caused by the rate dependent parameters of the SC-15 matrix material. The SC-15 matrix material transitions from a "ductile" to a "brittle" material as the rate increases. This change causes a transition in the composite material response and failure.

The weft direction shows similar results, see figure 14, however, the model is able to capture more accurately the formation of the kink band and the angle which it would occur through the specimen. Again the locations of the Z-fibers provides a source for the kink band initiation and propagation path. This would suggest that the single RUC approach can more accurately capture the failure of the weft direction than that of the warp direction. The transition in failure mode was also accurately captured as the quasi-static response predicts kink band formation while the dynamic response was seen to predict brooming and delamination, as described in Pankow, Waas, Yen, and Ghiorse (2012); Pankow, Salvi, Waas, Yen, and Ghiorse (2011).
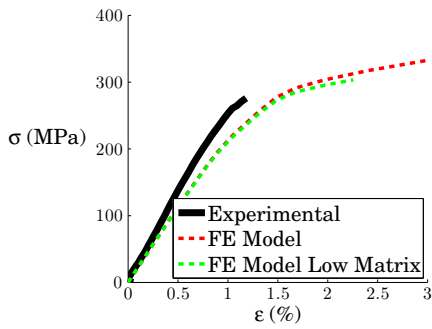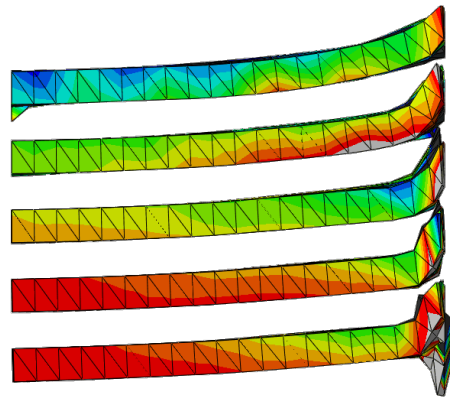
(a) Global stress vs. strain response
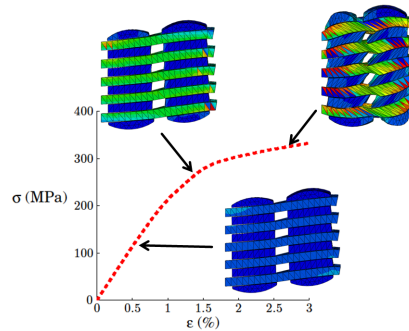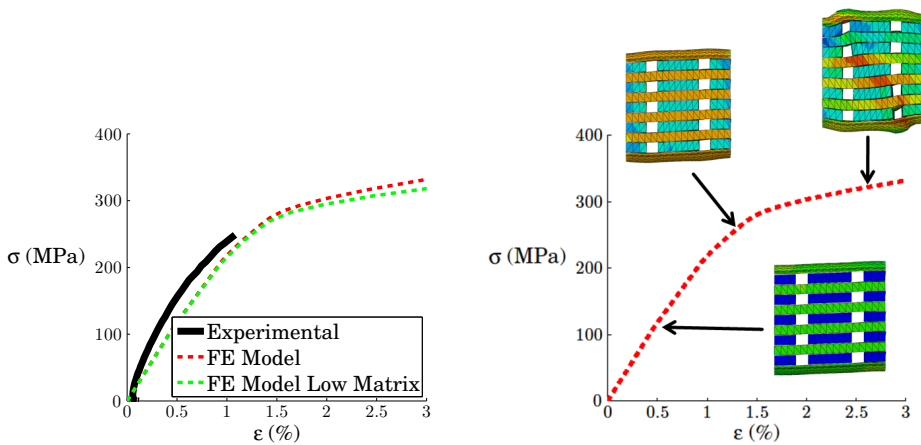

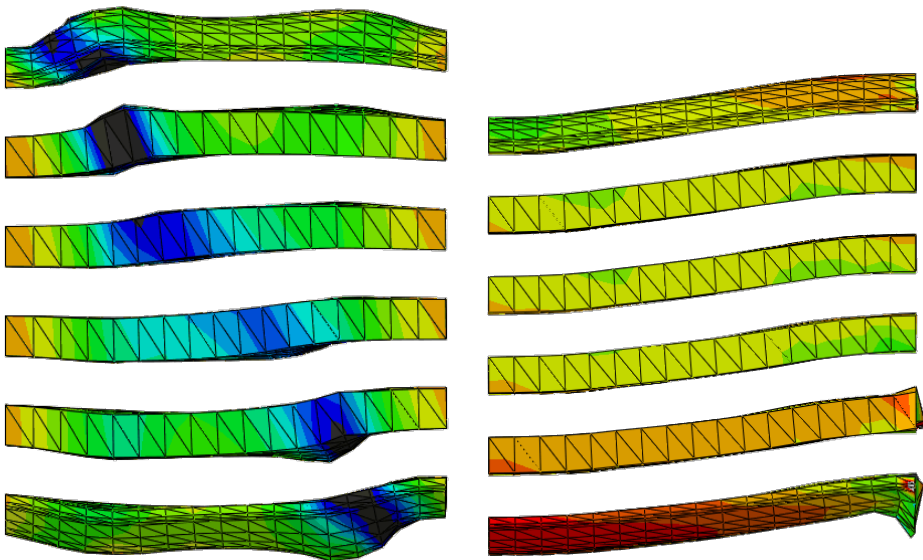(b) Evolution of deformed shape
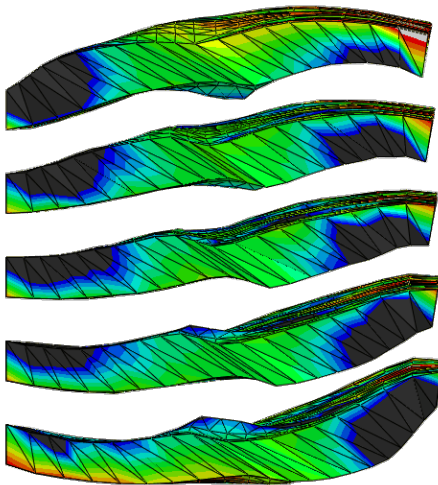
(c) Static

(d) Dynamic

Figure 13: Macroscopic stress vs. macroscopic strain response comparison of static results in the warp direction. Low matrix refers to the matrix yield strength being cut in half. Von Mises strain contours are shown.

(a) Global stress vs. strain

(b) Evolution of deformed shape

(c) Static

(d) Dynamic

Figure 14: Macroscopic stress vs. macroscopic strain response comparison of static results in the weft direction. Low matrix refers to the matrix yield strength being cut in half. Von Mises strain contours are shown.

Since the warp direction simulations could not accurately capture the details of the kink band angle, a more refined mesh was examined to determine if this was a result of mesh sensitivity or if it was related to the number of RUC's in the model. A higher density mesh was used with 304,000 elements as compared to the previous 70,000 elements. The macroscopic stress vs. strain responses are shown in figure 15, which shows that the results do not change with an increase in mesh density. However, the actual mode shape, associated with fiber tow bending and shearing, changes as the model has a better ability to capture these deformations seen in the experimental results. This comparison can be seen in figure 15, which shows a comparison of the two deformed mode shapes. With a higher mesh density the modes are more accurately predicted. The Z-fiber provides a source of kink band formation. These results show the role these fibers play in the onset of failure in the material. However, as can be seen, the kink band does not form at the angle observed in the post-experiment microscopic images - experiments show an angle of about 45°, while the predictions are at 75° (see figures 6, 11, and 15). This lack in fidelity is related more to the number of repeat units in the RVE, since the kink band will originate from the Z-fiber and travel further out, as indicated by the path "AB" in figure 16. Thus, a multiple RVE model must be created to capture the details of the kink band formation.

6   Multiple RUC Static Tests

The simulations reported in this section will contain four unit cells within a "super RVE" which we shall refer to as a SRVE. The SRVE model has 92,000 elements. This provides a similar mesh density to the initial model used. All of the properties described earlier are used again in this model, however R_{11} was reset to its original value of 25. The same boundary conditions that were imposed on the single RUC have been implemented in the SRVE.

The SRVE model was again perturbed to seed an initial geometric imperfection. Two different types of perturbations were used. The first type allowed for movement in any direction, during the buckling mode extraction. The buckling mode shape is shown in figure 17(a). A second type was obtained by preventing out of plane deformation at the end during the buckling mode extraction. This caused a different type of buckling mode as shown in figure 17(b). Both these modes were used to perturb the SRVE and to examine compressive response.

The amplitude of imperfection was varied to determine its effect on the peak load. Figure 19 shows the correlations between the different models (referred to as "confined" and "unconfined"). The initial imperfection amplitude for the unconfined model was 8.76% and the confined model amplitude was 5.88%. A comparison of the amount of imperfection vs the max stress is shown in figure 18. The confined
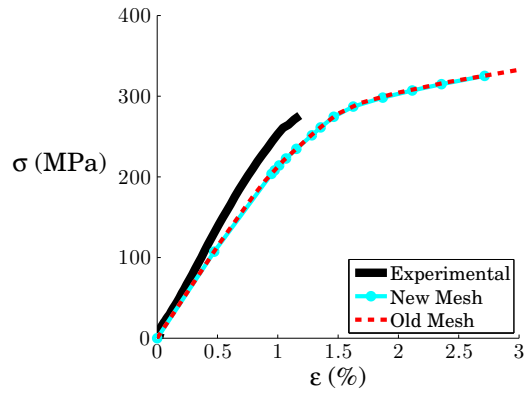
(a)
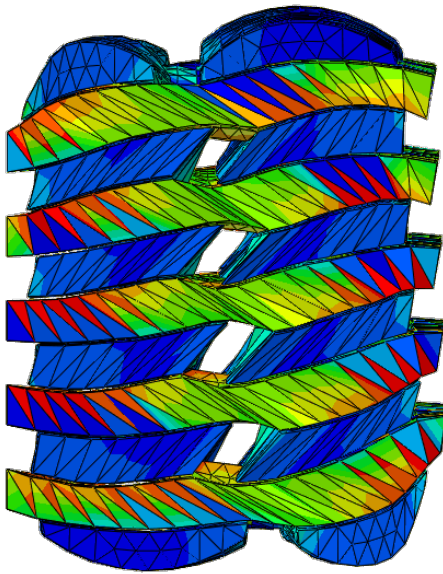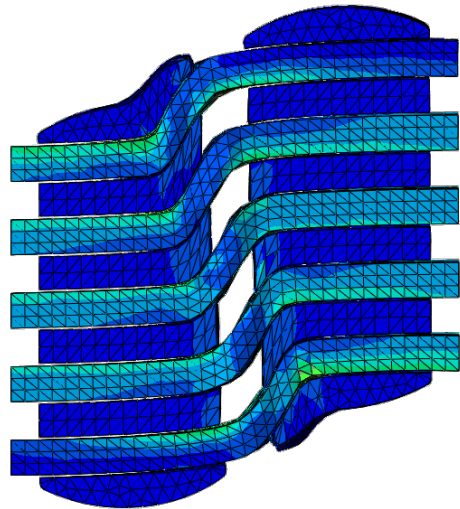
(b)   (c)
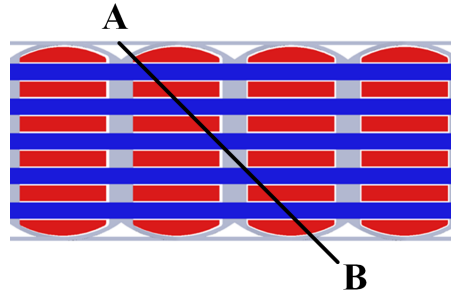
Figure 15: Comparison of Mesh on Computational Results.

Figure 16: Required path for proper kink band formation in RUC model. Note that it will travel across multiple Z-fibers during formation

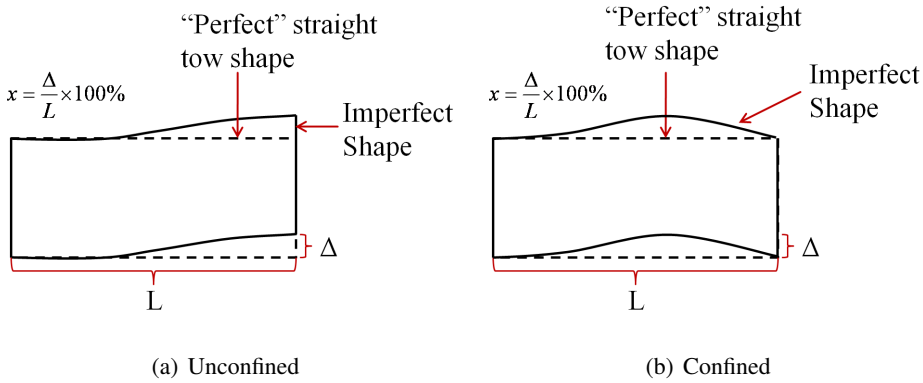(a) Unconfined   (b) Confined

Figure 17: Amplitude perturbation to seed initial imperfection.

specimen failed at a smaller imperfection amplitude. The plasticity of the matrix had very little influence on the failure load as was shown previously in the single RUC example. Both models are able to more accurately capture the kink band formation that forms at an angle of about 45° in the specimen. Therefore the warp direction needs the additional unit cells to capture the correct details of the kink banding failure mechanism since it bridges the Z-fiber locations. This would suggest that at least two full z-fibers would need to be modeled to accurately capture kink band formation. Additionally, it is noted that the relatively coarse mesh of the model was able to capture both the kink band formation and also the response of the material, fairly accurately.

Overall both models are able to predict certain aspects of the experimental results. The modeling strategy adopted here, which is similar to the ones used earlier in
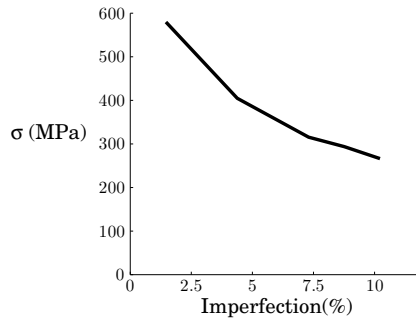
Figure 18: Comparison of imperfection to max strength for unconfined specimen.

Song, Waas, Shahwan, Xiao, and Faruque (2007), is able to capture tow kink banding, naturally emerging as a result of material nonlinearity and geometric nonlinearity, both of which are essential to capture a limit load type instability.

7   Conclusions

Quasi-static simulations of 3D woven composite materials have been reported. The modeling strategy, which involves homogenized elastic-plastic tows within an elastic-plastic matrix, has been shown to capture the salient features of experimental results for two directions (warp and weft) of compressive loading. The same modeling strategy was used earlier by the authors, and it was shown to correctly capture high rate compressive response as reported in Pankow, Waas, Yen, and Ghiorse (2012). Thus, the computational model is able to predict compressive response and onset of failure at both quasi-static and elevated strain rates. The model also predicts the transition in failure mode as a function of textile architecture. The single RUC representation was found to predict the failure stress correctly, while it did not capture the details of the kink band angle. Thus, a multiple RUC representation was implemented and this larger model was found to predict both the failure mode and the peak stress accurately. Therefore, the multiple RUC models are needed to correctly capture details of the failure mechanism and the peak stress in modeling compressive response.

(a)

(b) Unconfined
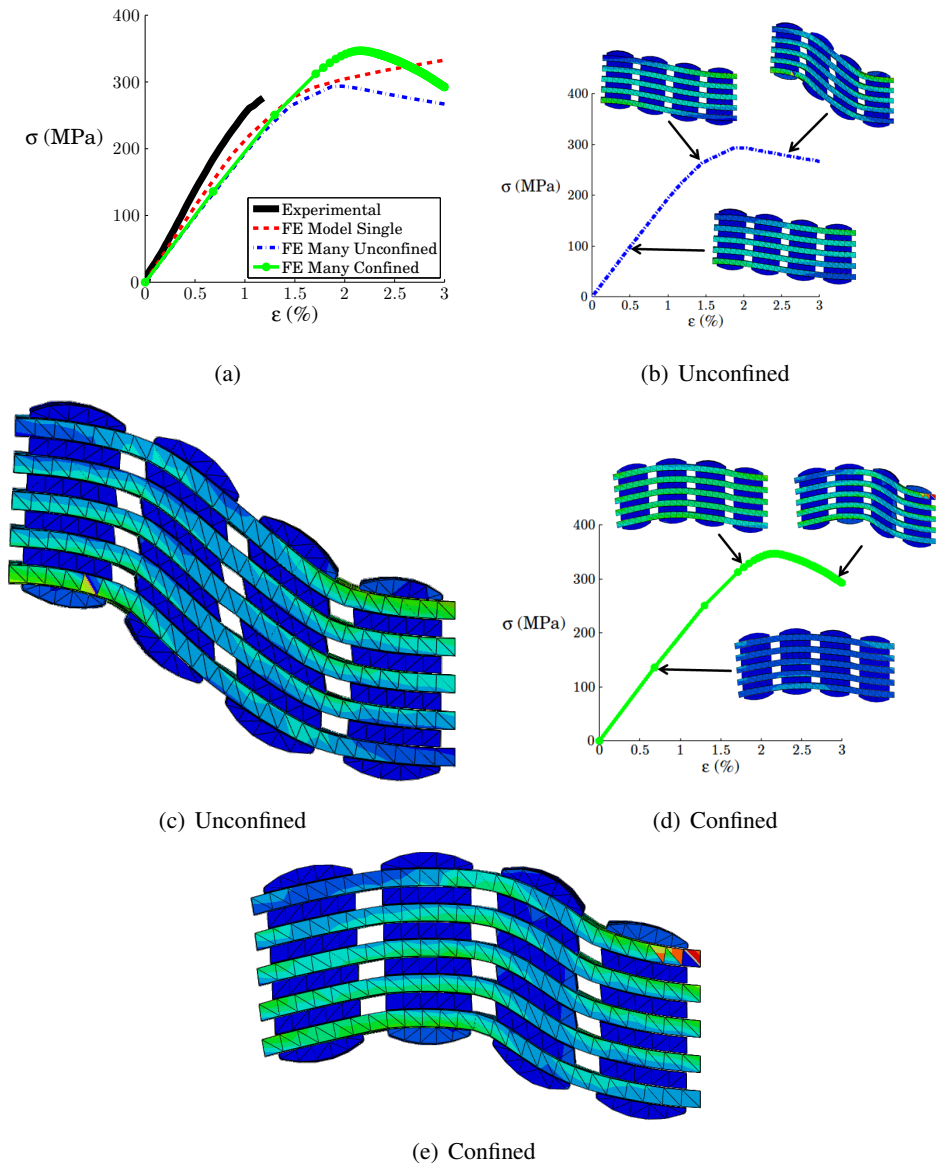

(c) Unconfined

(d) Confined

(e) Confined

Figure 19: Macroscopic stress vs. macroscopic strain response comparison of static results comparing the different models. Von Mises strain contours are shown.

References

Bogdanovich, A.; Mohamed, M. (2009):   Three-dimensional reinforcemets for composites. *SAMPE*, vol. 45, no. 6, pp. 8–28.

Herakovich, C. (1998):   *Mechanics of Fibrous Composites*. McGraw-Hill, New York, 2 edition.

Ji, K.; Kim, S. (2007):   Dynamic direct numerical simulation of woven composites for low-velocity impact. *Journal of Composite Materials*, vol. 41, pp. 175–200.

Jones, R. (1999):   *Mechanics of Composite Materials*. Taylor and Francis.

Kamiya, R.; Cheeseman, B.; Popper, P.; Chou, T. (2000):   Some recent advances in the fabrication and design of three-dimensional textile preforms: a review. *Composites Science and Technology*, vol. 60, pp. 33–47.

Lomov, S.; Ivanov, D.; Verpoest, I.; Zako, M.; Kurashiki, T.; Nakai, H.; Hirosawa, S. (2007):   Meso-fe modeling of textile composites: Road map, data flow and algorithms. *Composites Science and Technology*, vol. 67, no. 9, pp. 1870–1891.

McGlockton, M.; Cox, B.; McMeeking, R. (2003):   A binary model of textile composites: Iii high failure strain and work of fracture in 3d weaves. *Journal of the Mechanics and Physics of Solids*, vol. 51, pp. 1573–1600.

Pankow, M.; Waas, A.; Yen, C.; Ghiorse, S. (2012):   Modeling the response, strength and degradation of 3d woven composites subjected to high rates of loading. *Composites Structures*, vol. 94, no. 5, pp. 1590–1604.

Pankow, M.; Salvi, A.; Waas, A.; Yen, C.; Ghiorse, S. (2011):   Split hopkinson pressure bar testing of 3d woven composites. *Composites Science and Technology*, vol. 71, pp. 1196–1208.

Pankow, M.; Waas, A.; Yend, C.; Ghiorse, S. (2009):   A new lamination theory for layered textile composites that account for manufacturing induced effects. *Composites Part A: Applied Science and Manufacturing*, vol. 40, no. 12, pp. 1991–2003.

Quek, S.; Waas, A. (2003):   Micromechanical analyses of instabilities in braided glass textile composites. *AIAA Journal*, vol. 41, pp. 2069–2076.

Quek, S.; Waas, A.; Shahwan, K.; Agaram, V. (2003):   Analysis of 2d triaxial flat braided textile composites. *International Journal of Mechanical Sciences*.

Quek, S.; Waas, A.; Shahwan, K.; Agaram, V. (2004):   Compressive response and failure of braided textile composites: Part 2 - computations. *International Journal of Non-Linear Mechanics*, vol. 39, pp. 649–663.

Raju, I.; Wang, J. (1994):   Classical laminate theory models for woven fabric composites. *Journal of Composites Technology and Research*, vol. 16, no. 4, pp. 289–303.

Robitaille, F.; Long, A.; Jones, I.; Rudd, C. (2003):   Automatically generated geometric descriptions of textile and composite unit cells. *Composites: PartA*, vol. 34, pp. 303–312.

Schwer, L.; Whirley, R. (1999):   Impact of a 3d woven textile composite thin panel: Damage and failure modeling. *Mechanics of Composite Materials and Structures*, vol. 6, pp. 9–30.

Sejnoha, M.; Zeman, J. (2008):   Micromechanical modeling of imperfect textile composites. *International Journal of Engineering Science*, vol. 46, pp. 513–526.

Shahkarami, A.; Vaziri, R. (2007):   A continuum shell finite element model for impact simulation of woven fabrics. *Internationl Journal of Impact Engineering*, vol. 34, pp. 104–119.

Song, S. (2007):   *Compression Response of Tri-Axially Braided Textile Composites*. PhD thesis, University of Michigan, 2007.

Song, S.; Waas, A.; Shahwan, K.; Faruque, O.; Xiao, X. (2008):   Compression response of 2d braided textile composites: Single cell and multiple cell micromechanics based strength strengh preditctions. *Journal of Composite Materials*, vol. 42, no. 23, pp. 2461–2482.

Song, S.; Waas, A.; Shahwan, K.; Faruque, O.; Xiao, X. (2009):   Compression response, strength and post-peak response of an axial fiber reinforce tow. *International Journal of Mechanical Sciences*, vol. 51, pp. 491–499.

Song, S.; Waas, A.; Shahwan, K.; Xiao, X.; Faruque, O. (2007):   Braided textile composites under compressive loads: modeling the response, strength and degradation. *Composites Sceince and Technology*, vol. 67, pp. 3059–3070.

Talbi, N.; Batti, A.; Ayad, R.; Guo, Y. (2009):   An analytical homogenization model for finite element modelling of corrugated cardboard. *Composite Structures*, vol. 88, pp. 280–289.

Tan, P.; Steven, G. (1997):   Modelling for predicting the mechanical properties of textile composites - a review. *Composites: Part A*, vol. 28A, pp. 903–922.

Tan, P.; Tong, L.; Steven, G. (1998):   Modelling approaches for 3d orthogonal woven composites. *Journal of Composite Materials*, vol. 17, pp. 545–577.

Tan, P.; Tong, L.; Steven, G. (2000):   Behavior of 3d orthogonal woven cfrp composites. part ii. fea and analytical modeling approaches. *Composites: Part A*, vol. 31, pp. 273–281.

Tan, P.; Tong, L.; Steven, G.; Ishikawa, T. (2000):   Behavior of 3d orthogonal woven cfrp composites part ii. fea and analytical modeling approaches. *Composites: Part A*, vol. 31, pp. 273–281.

Yen, C.; Caiazzo, A. (2001):   3d woven composites for new and innovative impact and penetration resistant systems. Technical Report MSC TPR 1015/CD01, U.S. Army Research Office, 2001.

Zeng, T.; Wu, L.; Guo, L. (2004):   Mechanical analysis of 3d braided composites: a finite element model. *Composite Structures*, vol. 64, pp. 399–404.